

Masako Sugihara-Seki and Hiroshi Yamada

Abstract

While considering the circulatory system, a mechanical view point provides the basis for understanding various physiological and pathophysiological phenomena. In this section, we introduce the fundamentals of fluid and solid mechanics in relation to the circulatory system. In the first part on fluid mechanics, we start by introducing the concepts of Newtonian and non-Newtonian fluids, viscosity, and apparent viscosity. Then, the rheological properties of blood are described, and the universal mechanical law for flow through cylindrical tubes is derived. Based on that law, we consider the characteristics of tube flow for Newtonian and non-Newtonian fluids and present several representative examples of mathematical models for blood flow through vessels. These models have a close relationship with important physiological phenomena. In the second part, we first discuss the concept of continuum mechanics for a large deformation of the vascular wall. Then, we introduce passive hyperelastic models, an active smooth muscle model, and incorporations of residual strain and smooth muscle contractions. We demonstrate typical axisymmetric solutions of arterial wall stress for a tube model under physiological loading conditions, i.e., longitudinal stretch and intraluminal pressure. We also show some approaches for arterial diseases such as atherosclerosis, aortic aneurysm, and aortic dissection.

Keywords

Apparent viscosity • Blood flow • Boundary-value problem • Continuum mechanics • Constitutive equation

M. Sugihara-Seki (✉)

Department of Pure and Applied Physics, Kansai University, Suita, Japan

e-mail: sekim@kansai-u.ac.jp

H. Yamada

Department of Biological Functions Engineering, Graduate School of Life Science and Systems Engineering, Kyushu Institute of Technology, Kitakyushu, Japan

2.1 Vascular Fluid Mechanics

In this section, we introduce the basic concepts of fluid mechanics to understand the circulatory system from a mechanics standpoint. Focusing on steady flow through circular cylindrical tubes, we describe the rheological behaviors of Newtonian and non-Newtonian fluids, and consider several distinctive features of blood flow through vascular vessels by utilizing simple mathematical models.

2.1.1 Newtonian and Non-Newtonian Fluids

First, the definition of “stress” in a fluid will be introduced. Suppose a small surface, S , is inside the fluid, and a unit vector normal to this surface is denoted as \mathbf{n} . As shown in Fig. 2.1, the fluid on the side of the surface, to which the normal vector points, exerts a force, \mathbf{F} , on this surface. In mechanics, the term “stress” is used to express force per unit area. Thus, the stress acting on this side of the surface, $\boldsymbol{\sigma}_n$, is defined as \mathbf{F}/S as the limit of S approaches 0. The stress acting on the other side of the surface is expressed as $-\mathbf{F}/S$ in the same limit, as may be understood by Newton’s third law. The stress has three components in space that depend on the location and orientation of the normal vector \mathbf{n} . In this sense, the stress can be specified by the so-called stress tensor of rank 2 (For details, refer to a text book of fluid mechanics, e.g., Farber 1995).

It is usually convenient to decompose stress, $\boldsymbol{\sigma}_n$, into a normal stress, normal to the surface or parallel to the vector \mathbf{n} , and a tangential stress, tangent to the surface, as shown in Fig. 2.1. The normal stress is sometimes called the tension if it works in the direction of \mathbf{n} , whereas it is called the pressure if it works in the opposite direction of \mathbf{n} .

2.1.1.1 Viscosity and Apparent Viscosity

As may be expected, only pressure acts on a fluid at rest. When the fluid flows, tangential stress is also generated. With regard to this issue, Newton first introduced the concept of “viscosity” of a fluid, utilizing a simple flow configuration sketched in Fig. 2.2.

Fig. 2.1 Force \mathbf{F} exerted on a surface, S , in a fluid

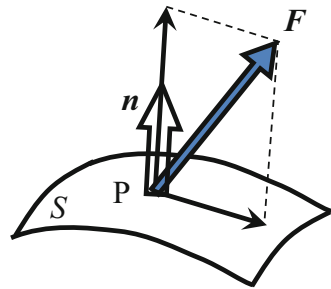
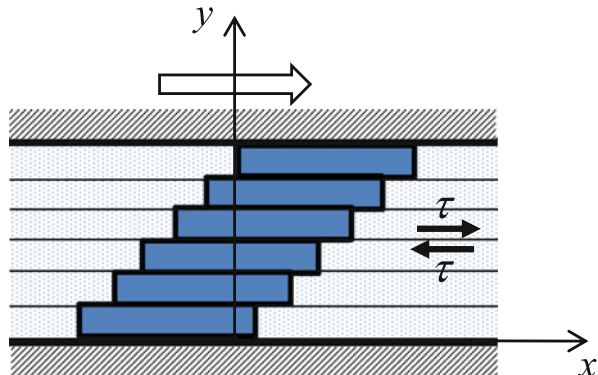


Fig. 2.2 Couette flow between two parallel plates



Suppose that a fluid is confined between two parallel plates, an upper plate that moves with a constant velocity and a lower plate that is stationary. Following the movement of the upper plate, planar laminae of the fluid lying parallel to the plates move steadily and slide over one another creating a uniform velocity gradient (or shear rate), $\dot{\gamma}$. Newton postulated that in such circumstances, a frictional shear stress (tangential stress) arises between adjacent laminae, the magnitude of which is proportional to the velocity gradient:

$$\tau = \eta \dot{\gamma}. \quad (2.1)$$

The proportional constant, η , is called the viscosity or shear viscosity. For homogeneous fluids such as water or saline, η is a material constant if temperature and pressure are specified. These fluids are referred to as Newtonian. Equation (2.1) is called the Newton formula. More rigorously, a Newtonian fluid is one in which the stress tensor in the fluid is a linear function of the rate of strain tensor, the components of which are expressed in terms of velocity gradients (e.g., Farber 1995).

In Fig. 2.2, the lamina next to the plate exerts the shear stress expressed by Eq. (2.1) on the plate. Thus, to keep the movement of the upper plate steady, we need to apply an external force on the plate that balances such a tangential force over the plate. Accordingly, if the force applied to the upper plate is measured, the fluid viscosity, η , can be estimated using Eq. (2.1). This is the principle used by rotational viscometers to measure viscosity of a fluid.

A fluid not obeying the Newton formula (2.1) is referred to as non-Newtonian. Blood plasma is generally regarded as a Newtonian fluid. Blood, however, behaves as a non-Newtonian fluid; the shear stress, τ , is a nonlinear function of $\dot{\gamma}$. Before studying blood viscosity, let us consider some representative characteristics of non-Newtonian fluids.

2.1.1.2 Representative Types of Non-Newtonian Fluids

A number of complex fluids, including whole blood, suspensions and slurries of rigid and deformable solid matter, and pastes and emulsions, are non-Newtonian. If

measurements of the shear stress, τ , and shear rate, $\dot{\gamma}$, are made for the flow configuration shown in Fig. 2.2, the ratio of these quantities defines a function, which is called apparent viscosity:

$$\eta_a(\dot{\gamma}) = \frac{\tau}{\dot{\gamma}}. \quad (2.2)$$

Although the apparent viscosity is not a material constant, it represents a rheological characteristic of the complex fluid.

Non-Newtonian fluids may be classified depending on the variation of the shear stress with shear rate or on the variation of the apparent viscosity with shear stress or shear rate. Figure 2.3 shows several representative behaviors of non-Newtonian fluids as well as that of Newtonian fluids (line (i)). The materials corresponding to lines (ii), (iii), and (iv) in Fig. 2.3 are called “Bingham plastic,” “pseudoplastic,” and “dilatant,” respectively. Bingham plastic does not deform at all when subjected to a shear stress smaller than a certain value. This is mostly due to the presence of microstructures or clusters of molecules, and a certain stress is required to break them. This critical value is called the “yield stress.” For stresses above the yield stress, the Bingham plastic flows with the shear stress as a linear function of shear rate. The pseudoplastic (line (iii)) exhibits a decrease in apparent viscosity as the shear rate increases. This phenomenon is sometimes called “shear-thinning.” Many materials, such as various polymer solutions, show pseudoplastic behavior in varying degrees. There are some materials that appear to expand when subjected to shear stresses; the dilatant (line (iv)) exhibits an increase in apparent viscosity as the shear rate increases because of this dilation. This phenomenon is sometimes called “shear-thickening,” and some concentrated suspensions of solids, slurries, and proteins show dilatant behavior.

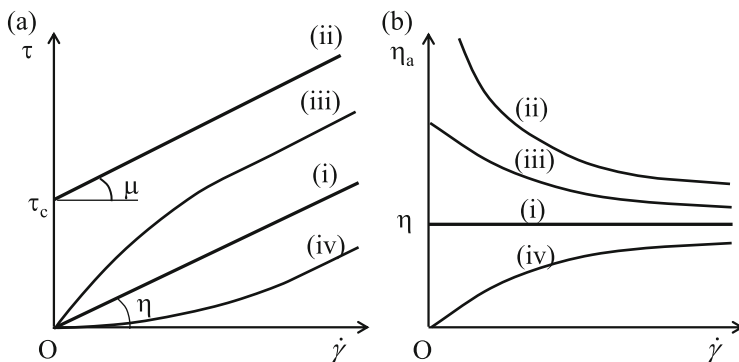


Fig. 2.3 Rheological properties of various types of fluids: (a) shear stress and (b) apparent viscosity vs shear rate for (i) Newtonian, (ii) Bingham plastic, (iii) pseudoplastic, and (iv) dilatant

It is evident that the straight line (i) in Fig. 2.3a for a Newtonian fluid is described by Eq. (2.1). The slope of this line corresponds to the viscosity, η . The line (ii) for Bingham plastic is expressed by

$$\begin{cases} \tau = \tau_c + \mu \dot{\gamma} & (\tau \geq \tau_c) \\ \dot{\gamma} = 0 & (\tau < \tau_c) \end{cases}, \quad (2.3)$$

where τ_c represents the yield stress, and μ is the plastic viscosity. The shear-thinning and shear-thickening may be ideally expressed by the so-called power-law fluid:

$$\tau = k \dot{\gamma}^n, \quad (2.4)$$

where n and k are constant, and $n < 1$ and $n > 1$ represent the shear-thinning and shear-thickening, respectively. $n = 1$ represents the Newtonian fluid. Equations (2.1), (2.3), and (2.4) specify the properties of the materials and are collectively called the constitutive equation.

2.1.2 Blood Viscosity

Blood is a suspension of red blood cells (erythrocytes), white blood cells (leukocytes), and platelets in plasma. Plasma is about 90 % water by weight, 7 % plasma protein, 1 % inorganic substances, and 1 % other organic substances. Normally, plasma is an incompressible Newtonian fluid with a viscosity of about 1.2 cP at 37 °C. The red cells constitute the largest percentage of cells with a hematocrit (volume fraction of red cells) of about 40–45 % in normal blood. The white cells of various categories make up less than 1/600th of the total cellular volume, and the platelets occupy less than 1/800th of the cellular volume (Fung 1993). Thus, blood can be regarded as a highly concentrated suspension of red cells, and its rheological properties are strongly influenced by these red cells.

The viscosity of blood at a given temperature is a function of shear rate, hematocrit, plasma viscosity, physical properties of the red cells, and cell aggregation. At a normal state of 45 % hematocrit, the apparent viscosity of whole blood is about 4 cP at relatively high shear rates. The relationship between the apparent viscosity, η_a , and hematocrit is nonlinear, with η_a rising at an increasing rate as the hematocrit increases.

Human red cells can form aggregates under low-flow conditions. They can deform when subjected to shear. Figure 2.4 is a typical diagram used to show the importance of red cell deformation and aggregation (Chien 1970). The apparent viscosities relative to the medium viscosity are shown for three different red cell suspensions, NP, NA, and HA. The line NP refers to normal blood. When the shear rate increases, blood aggregates tend to be broken up, and the viscosity of blood decreases. As the shear rate further increases, the deformation of the red cells becomes more evident, and the red cells are elongated and aligned with the flow

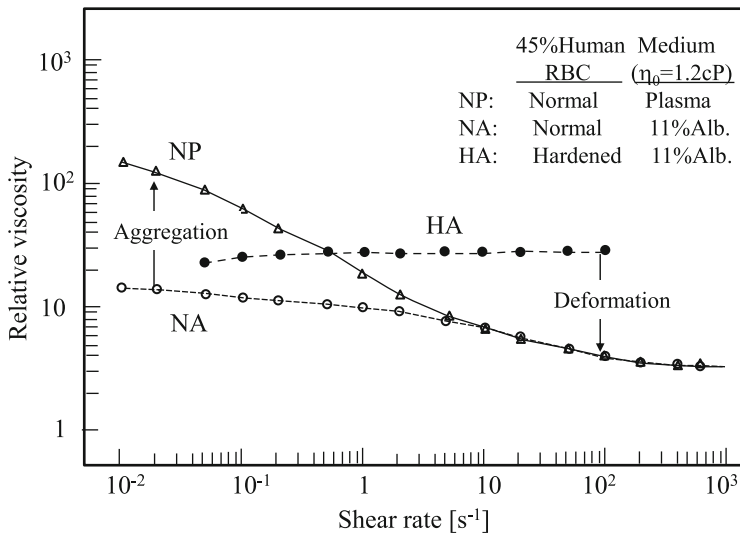


Fig. 2.4 Logarithmic relation between viscosity and shear rate in three types of suspensions at 37 °C, each containing 45 % human RBC by volume (Modified from Chien 1970)

direction, which reduces blood viscosity. The line NA refers to a suspension of normal red cells in isotonic saline containing 11 % albumin, and they show deformation but no aggregation. The third line, HA, refers to a suspension of hardened red cells in the same saline solution, and they show neither deformation nor aggregation. At low shear rates, the apparent viscosity relative to the medium viscosity is higher for NP than for NA because of red cell aggregation, and at high shear rates it is lower for NP than for HA because of red cell deformation.

It is convenient to have analytical expressions representing the blood apparent viscosity as a function of rheological factors such as hematocrit and shear rate. A number of equations have been proposed to describe the rheological behavior of blood. Among them, Scott-Blair (1959) used Casson equation derived by Casson (1959) based on a mechanical model of suspension flow:

$$\sqrt{\tau} = \sqrt{\tau_c} + \sqrt{\eta_c} \sqrt{\dot{\gamma}}, \quad (2.5)$$

where η_c and τ_c are called the Casson viscosity and Casson yield stress, respectively. In this model, the suspension was assumed to contain particles that can aggregate at low shear rates to form rod-like aggregates, which increase in length as the shear rate decreases. Scott Blair plotted $\tau^{1/2}$ against $\dot{\gamma}^{1/2}$ for whole blood, plasma, and serums of several species and showed that they produced excellent straight lines. Cokelet et al. (1963) showed that for small shear rates, $\dot{\gamma} < 10 \text{ s}^{-1}$, and for a hematocrit less than 40 %, the blood viscosity is well described by the Casson Eq. (2.5).

It is generally accepted that blood does not flow unless the shear stress exceeds yield stress, τ_c , the value of which is markedly influenced by several factors such as hematocrit and macromolecular composition. Since τ_c is very small, ~ 0.05 dyn/cm² (Merrill et al. 1963), experimental determination of yield stress is complicated. It is known that a suspension of red cells in plasma containing fibrinogen has a finite yield stress, but a suspension of red cells in saline plus albumin has zero yield stress. At high shear rates, whole blood behaves like a Newtonian fluid with a constant viscosity.

2.1.3 Steady Flow Through Circular Cylindrical Tubes

As a basis to understand blood flow through vascular vessels, we consider the steady laminar flow of a homogeneous fluid through a straight circular cylindrical tube of radius R and length L under a pressure difference, Δp . Since the tube radius is uniform, it is reasonable to assume that the flow is parallel to the cylindrical axis, the x -axis. In this section, we derive an expression for shear stress in the fluid using the property that the net force acting on any fluid element vanishes because of steady flow.

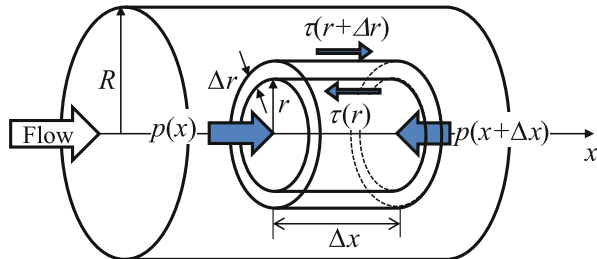
We consider a fluid element of circular cylindrical annulus of radius r , thickness Δr and length Δx , the center of which lies on the centerline of the tube, as shown in Fig. 2.5. If shear stresses acting on the circumferential surfaces of the annulus at $r = r$ and $r + \Delta r$ are expressed as $\tau(r)$ and $\tau(r + \Delta r)$, respectively, then the total force exerted on the circumferential surfaces becomes

$$\tau(r + \Delta r) \times 2\pi(r + \Delta r)\Delta x - \tau(r) \times 2\pi r\Delta x \quad (2.6)$$

in the x -direction. This force is balanced with the pressure difference exerted at both ends of the cylindrical annulus at $x = x$ and $x + \Delta x$. This condition of force balance yields

$$[(r + \Delta r)\tau(r + \Delta r) - r\tau(r)] 2\pi\Delta x = [p(x + \Delta x) - p(x)] 2\pi r\Delta r. \quad (2.7)$$

Fig. 2.5 A fluid element of circular cylindrical annulus of radius r , thickness Δr , and length Δx



Using Taylor expansions, we obtain

$$-\frac{dp}{dx} + \frac{1}{r} \frac{d}{dr}(r\tau) = 0. \quad (2.8)$$

Integration of this equation in the r -direction leads to

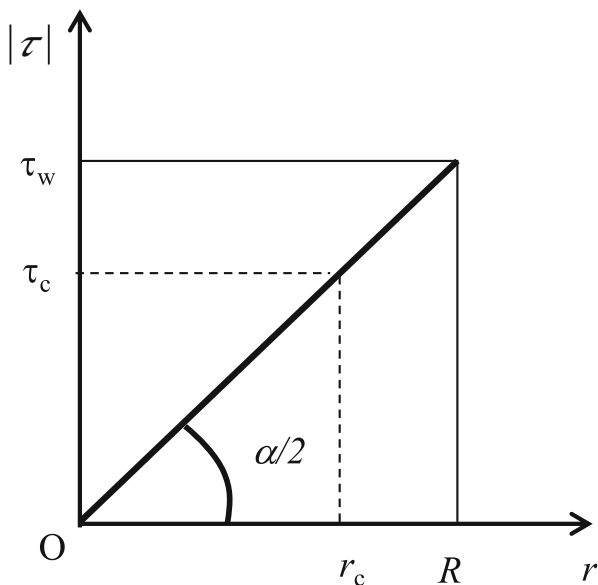
$$\tau = -\frac{\alpha}{2}r + \frac{C}{r}, \quad (2.9)$$

where $\alpha = -dp/dx = \Delta p/L$ represents the pressure gradient, and C is a constant. Since the shear stress is finite at $r=0$, C is determined to be 0, and the shear stress at the radial position r is obtained as

$$\tau = -\frac{\alpha}{2}r. \quad (2.10)$$

The magnitude of shear stress is illustrated in Fig. 2.6. It vanishes at the centerline of the tube and increases linearly with r up to a maximum value, $\tau_w (= \alpha R/2)$, on the tube wall. Equation (2.10) is valid for both Newtonian and non-Newtonian fluids. Next, we obtain a velocity profile for several types of fluids based on this relationship (2.10).

Fig. 2.6 Magnitude of shear stress in a steady tube flow. The shear stress reaches the yield stress τ_c at radial distance r_c



2.1.3.1 Flow of Newtonian Fluids

We consider the flow of a Newtonian fluid with viscosity η through a cylindrical tube treated above. Since velocity gradient in this case is expressed as du/dr , Eq. (2.1) is rewritten as

$$\tau = \eta \frac{du}{dr}. \quad (2.11)$$

Thus, substituting Eq. (2.11) in Eq. (2.10) and integrating under the no-slip boundary condition on the tube wall yields the velocity profile in the tube:

$$u = \frac{\alpha}{4\eta} (R^2 - r^2). \quad (2.12)$$

Equation (2.12) represents a parabolic velocity profile, called the Poiseuille flow. The flow rate per unit time is easily obtained as

$$Q = \int_0^R u 2\pi r dr = \frac{\pi R^4}{8\eta} \alpha. \quad (2.13)$$

For a given pressure gradient, $\alpha(=\Delta p/L)$, the flow rate Q is proportional to R^4 , indicating that it depends substantially on the tube radius. In other words, a small change in the tube radius drastically affects the flow rate through the tube. This may reflect effective control of blood flow in arterioles by changing their radii.

2.1.3.2 Flow of Casson Fluids

Next, let us consider the steady flow of a Casson fluid through a tube under the same condition. The constitutive Eq. (2.5) can be used if $\tau > \tau_c$. If not, the velocity gradient vanishes, i.e.

$$\dot{\gamma} = \frac{du}{dr} = 0. \quad (2.14)$$

Thus, we notice from Fig. 2.6 that if $\tau_w < \tau_c$, then the magnitude of the shear stress is smaller than τ_c in the entire region of the tube. In this case, Eq. (2.14) together with the no-slip boundary condition on the tube wall leads to

$$u = 0 \quad (\tau_w < \tau_c). \quad (2.15)$$

The condition of $\tau_w = \tau_c$ provides a critical pressure difference $(\Delta p)_c$ to generate fluid flow through the tube:

$$(\Delta p)_c = \frac{2\tau_c}{R} L. \quad (2.16)$$

If the pressure difference across the tube is smaller than $(\Delta p)_c$, flow does not occur.

For the case of $\tau_w > \tau_c$, we define the critical radius r_c by

$$\tau_c = \frac{\alpha}{2} r_c. \quad (2.17)$$

It can be seen from Fig. 2.6 that for $r > r_c$, the magnitude of shear stress is larger than τ_c for cases where Eq. (2.5) is satisfied. For $r < r_c$, the magnitude of shear stress is smaller than τ_c for cases where Eq. (2.14) is satisfied. Combining these equations and Eq. (2.10) yields

$$\begin{cases} \sqrt{\frac{\alpha}{2}}r = \sqrt{\tau_c} + \sqrt{\eta_c} \sqrt{-\frac{du}{dr}} & (r_c \leq r \leq R) \\ \frac{du}{dr} = 0 & (r < r_c) \end{cases}. \quad (2.18)$$

The second equation implies that the velocity profile is flat for $r < r_c$. From the first equation, we obtain

$$-\frac{du}{dr} = \frac{1}{\eta_c} \left(\sqrt{\frac{\alpha}{2}}r - \sqrt{\tau_c} \right)^2 \quad (r_c \leq r \leq R). \quad (2.19)$$

Integrating this equation and using the no-slip boundary condition on the tube wall at $r = R$, we have

$$u = \frac{\alpha}{4\eta_c} \left[R^2 - r^2 - \frac{8}{3} r_c^{1/2} (R^{3/2} - r^{3/2}) + 2r_c(R - r) \right] \quad (r_c \leq r \leq R). \quad (2.20)$$

Inserting $r = r_c$ into Eq. (2.20), we obtain the velocity u_c , which represents the constant velocity in the region $r < r_c$:

$$u_c = \frac{\alpha}{4\eta_c} \left(\sqrt{R} - \sqrt{r_c} \right)^3 \left(\sqrt{R} + \frac{1}{3}\sqrt{r_c} \right) \quad (r < r_c). \quad (2.21)$$

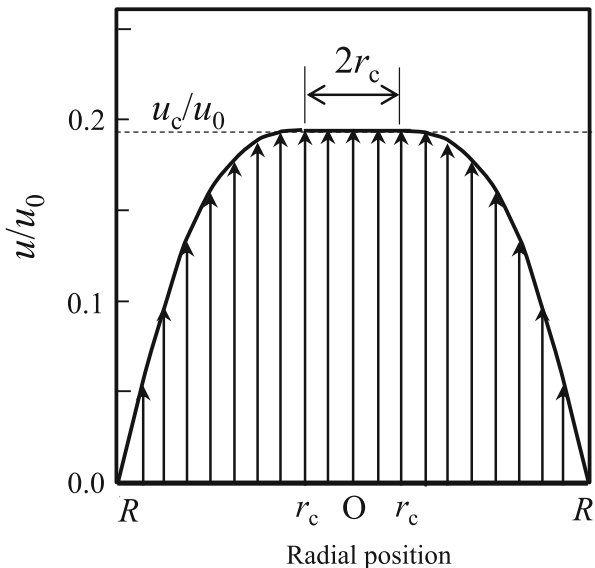
Equations (2.20) and (2.21) provide a blunt velocity profile as shown in Fig. 2.7. The flow rate is easily obtained as

$$Q = \frac{\pi R^4 \alpha}{8\eta_c} F(\xi) \quad (\tau_w > \tau_c), \quad (2.22)$$

where $F(\xi)$ was formulated by Oka (1981) as

$$F(\xi) = 1 - \frac{16}{7} \xi^{1/2} + \frac{4}{3} \xi - \frac{1}{21} \xi^4, \quad \xi = \frac{r_c}{R}. \quad (2.23)$$

Fig. 2.7 Velocity profile of a Casson fluid in a tube ($r_c/R = 0.2$). $u_0 = \alpha R^2/(4\eta_c)$



In the case of $r_c = 0$ or $\tau_c = 0$, as expected, Eqs. (2.20) and (2.22) reduce to Eqs. (2.12) and (2.13), respectively. In the other cases, since r_c is related to α (Eq. 2.17), the velocity profile and flow rate depend nonlinearly on pressure gradient.

Here, if we define $\eta_a = \eta_c/F(\xi)$, then Eq. (2.22) can be rewritten as

$$Q = \frac{\pi R^4}{8\eta_a} \alpha. \quad (2.24)$$

This equation has the same form as Eq. (2.13) for Poiseuille flow. The quantity η_a in Eq. (2.24) is also called apparent viscosity. From Eq. (2.23), we note that apparent viscosity for a Casson fluid increases rapidly with increasing ξ .

2.1.3.3 Flows of Bingham Plastic and Power-Law Fluids

It may be interesting to consider the flow of other types of non-Newtonian fluids in a tube. Here, we briefly treat a Bingham plastic and power-law fluid as representative examples.

For a Bingham plastic fluid with the constitutive equation given by Eq. (2.3), a straightforward calculation similar to Sect. 2.1.3.2 for a Casson fluid leads to the velocity profile and apparent viscosity under the condition of $\tau_c < \tau_w$:

$$u = \begin{cases} \frac{\alpha}{4\mu} [(R^2 - r^2) - 2r_c(R - r)] & (r_c \leq r \leq R) \\ \frac{\alpha}{4\mu} (R - r_c)^2 & (r < r_c) \end{cases}, \quad (2.25)$$

and

$$\eta_a = \mu \left[1 - \frac{4}{3}\xi + \frac{\xi^4}{3} \right]^{-1}, \quad \xi = \frac{r_c}{R}, \quad (2.26)$$

where r_c is defined by Eq. (2.17). Under the condition of $\tau_c > \tau_w$, there is no flow.

For a power-law fluid with the constitutive equation given by Eq. (2.4), we obtain the velocity profile and apparent viscosity:

$$u = u_0 \left(1 - \left(\frac{r}{R} \right)^{\frac{n+1}{n}} \right), \quad u_0 = \left(\frac{\alpha}{2k} \right)^{\frac{1}{n}} \frac{n}{n+1} R^{\frac{n+1}{n}}, \quad (2.27)$$

$$\eta_a = \frac{R^2 \alpha}{8u_0} \frac{3n+1}{n+1}. \quad (2.28)$$

Except for the case of $n = 1$, corresponding to a Newtonian fluid, the velocity profile as well as flow rate depend on the pressure difference in a non-linear fashion as a power of $1/n$.

2.1.4 Application to Various Blood Flows

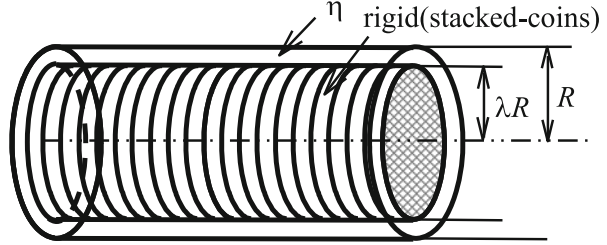
The basic ideas introduced above are helpful to understand several important and unique characteristics of blood flow through blood vessels. Here, we present some typical examples. In each case, an idealized model describes the distinct features of blood flow observed *in vivo* and predicts its physiological impact.

2.1.4.1 “Stacked-Coins” Model

The apparent viscosity of blood flowing through small vessels is known to be much smaller than the bulk viscosity of blood (Fahraeus-Lindqvist effect) (Fahraeus and Lindqvist 1931). Fluid mechanical investigations on this phenomenon are rather complicated, since the continuum approach considered so far may be inappropriate because of the comparable sizes of blood cells and vessel radii. Instead, we need to analyze the individual motion of the blood cells that interact with the surrounding plasma. However, the idea introduced at the beginning of this section is useful for conducting a simple analysis that accounts for the phenomena in small capillaries.

In a vessel with a diameter smaller than $\sim 6 \mu\text{m}$, red cells are most likely to flow in a single file, and a layer of plasma exists between the red cells and vessel wall. When the distance between neighboring cells is much smaller than vessel diameter, this flow situation may be described as the first approximation by the “axial-train” model developed by Whitmore (1968), depicted in Fig. 2.8, and also referred to as the “stacked-coins” model. In this model, the red cells are confined in a cylindrical core of radius λR that is concentric with the vessel and moves as a rigid body. The spacing between the core and vessel wall is assumed to be filled with plasma, a Newtonian fluid of viscosity η .

Fig. 2.8 Stacked-coins model



If we follow procedure similar to Sect. 2.1.3.1 for the plasma in the region of $\lambda R \leq r \leq R$, then we obtain Eq. (2.12) for the velocity profile of the plasma in the gap region. From the no-slip condition at the interface between red cells and plasma, putting $r = \lambda R$ in Eq. (2.12) provides the velocity of the stacked coins (red cell core):

$$u_c = \frac{R^2 \alpha}{4\eta} (1 - \lambda^2). \quad (2.29)$$

The flow rate of the whole blood including red cells and plasma is given by

$$Q = \frac{\pi R^4 \alpha}{8\eta} (1 - \lambda^4). \quad (2.30)$$

Thus, apparent viscosity of the stacked-coins model is given in terms of plasma viscosity, η , and radius ratio, λ , as

$$\eta_a = \frac{\eta}{1 - \lambda^4}. \quad (2.31)$$

This model may give some insight into the low viscosity observed in small capillaries. Equation (2.31) indicates that the presence of even a relatively thin layer of plasma in a capillary is sufficient to keep apparent viscosity at a reasonably low level. For instance, a plasma layer of $0.3 \mu\text{m}$ thickness in a capillary of diameter $6 \mu\text{m}$ gives $\lambda = 0.9$ and $\eta_a = 2.9\eta$, which is lower than the bulk viscosity of whole blood.

2.1.4.2 Capillary Flow in the Presence of a Glycocalyx Layer

Although it has long been known that the luminal surface of the vascular endothelium is lined with a layer of glycocalyx, it was not known until recently that this glycocalyx layer plays important roles in multifaceted endothelial functions such as microvessel permeability, regulation of blood flow, and blood cell interactions (Pries et al. 2000; Weinbaum et al. 2007). If the glycocalyx layer impedes the flow, the presence of the layer decreases the effective cross-sectional area of the vessel available for plasma and red cell motion, so it could possibly cause an increase in apparent viscosity as well as a decrease in hematocrit in small vessels.

These effects can be understood based on the same idea by using a mathematical model for the flow of a Newtonian fluid.

In the current model, we consider a circular cylindrical tube of radius R with a glycocalyx layer of constant thickness h lining the interior surface of the tube wall. Since the glycocalyx layer is composed of fiber matrixes, it can be assumed to be a porous material and the so-called ‘‘Darcy law’’ is applied. Thus, a frictional force proportional to the fluid velocity, $-Ku$, is exerted on the fluid per unit volume within the glycolcayx layer, where K denotes the hydraulic resistivity of the glycocalyx layer. Adding this frictional force term, $-Ku \cdot 2\pi r \Delta r \Delta x$, to the left-hand side of Eq. (2.7), we obtain, in place of Eq. (2.8), for the steady flow of a Newtonian fluid within the glycocalyx layer ($R - h \leq r \leq R$):

$$-\frac{dp}{dx} + \frac{1}{r} \frac{d}{dr}(r\tau) - Ku = 0 \quad (R - h \leq r \leq R). \quad (2.32)$$

Applying Eq. (2.32) for $R - h \leq r \leq R$ and Eq. (2.8) for $r < R - h$ together with the constitutive Eq. (2.1) for the Newtonian fluid, we obtain the velocity profile:

$$u = \begin{cases} \frac{\alpha}{K} \left[AI_0\left(\frac{r}{\delta}\right) + BK_0\left(\frac{r}{\delta}\right) + 1 \right] & (R - h \leq r \leq R) \\ \frac{\alpha}{4\eta}(-r^2 + C) & (r < R - h) \end{cases}, \quad (2.33)$$

where I_0 and K_0 are modified Bessel functions and $\delta = \sqrt{\eta/K}$. A , B , and C are constants expressed in terms of R , h , and δ (for details see Sugihara-Seki and Fu 2005). The dimension of δ is the length, and it represents a typical thickness to which the flow outside the layer penetrates within the layer.

Figure 2.9 illustrates the velocity profiles of Eq. (2.33) for $\delta = 0.02, 0.05, 0.1$, and $0.2 \mu\text{m}$, when the pressure gradient α is kept constant at $h = 0.5 \mu\text{m}$ and $R = 3 \mu\text{m}$. In this figure, the velocity is normalized by the centerline velocity of a Poiseuille flow at $K = 0$.

No direct measurements of the mechanical properties of the glycocalyx layer have been reported. However, observations of its functional behavior and theoretical considerations have given estimates that the value of K for the vascular endothelial glycocalyx layer is at least 10^{11} N s/m^4 or 10^{14} N s/m^4 , leading to $\delta \approx 0.01 - 0.1 \mu\text{m}$ (Pries et al. 2000; Weinbaum et al. 2003; Sugihara-Seki 2006). Figure 2.9 indicates that the fluid is almost stationary within the glycocalyx layer, so the presence of the glycocalyx layer is nearly equivalent to a decrease in the vessel radius from R to $R - h$. This result implies that the flow of Newtonian fluids exhibits an increase in apparent viscosity by $R^4/(R - h)^4$ times. For instance, a $0.5\text{-}\mu\text{m}$ thick glycocalyx in a $6\text{-}\mu\text{m}$ diameter capillary gives $R/(R - h) = 1.2$ and $R^4/(R - h)^4 \approx 2$, which is a significant increase in apparent viscosity. In addition, the presence of the glycocalyx layer causes a considerable decrease in the hematocrit in small vessels since red cells do not invade the glycocalyx layer under normal conditions.

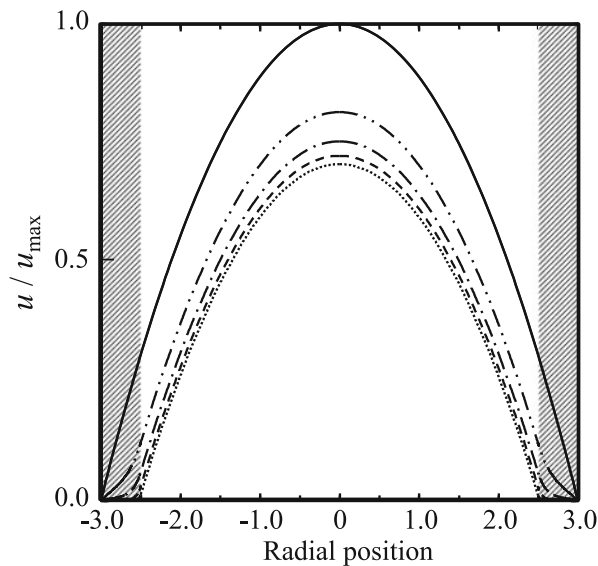


Fig. 2.9 Velocity profiles of a Newtonian fluid through a tube in the presence of a glycocalyx layer at its luminal surface ($h = 0.5 \mu\text{m}$, $R = 3.0 \mu\text{m}$). Dotted curve, $\delta = 0.02 \mu\text{m}$; dashed curve, $\delta = 0.05 \mu\text{m}$; dash-dotted curve, $\delta = 0.1 \mu\text{m}$; dash-double dotted curve, $\delta = 0.2 \mu\text{m}$. The solid curve represents the velocity profile of Poiseuille flow with the same pressure gradient α (Modified from Sugihara-Seki and Fu 2005)

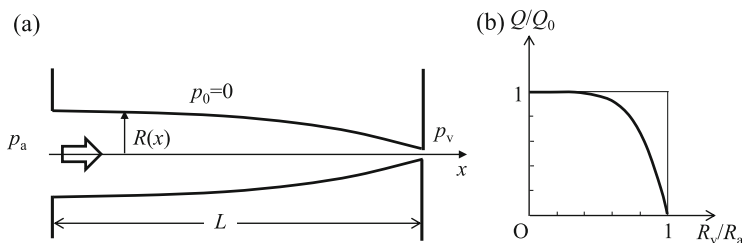


Fig. 2.10 The flow of a Newtonian fluid through an elastic tube. (a) Configuration and (b) relationship between flow rate and radius ratio

2.1.4.3 Steady Flow in an Elastic Tube

Another type of flow in circular cylindrical tubes to consider is the steady flow of a Newtonian fluid in an elastic tube when the upstream and downstream pressures are prescribed, as shown in Fig. 2.10a. The flow through distensible vessels was first analyzed in a model study for sheet flow in pulmonary alveolar blood vessels (Fung and Sobin 1972).

We assume that the cross section of the tube is maintained in a circular shape, and the radius of the tube is governed by the pressure difference between the inside and outside of the tube, $p - p_0$, in such a way that

$$R = R_0 + k(p - p_0), \quad (2.34)$$

where R_0 and k are constants. The pressure p_0 represents the external pressure; we assume $p_0 = 0$ hereafter, without the loss of generality. We further assume that the radii of the tube vary gradually in the flow direction along the x -axis, so that Eqs. (2.12) and (2.13) for Poiseuille flow can apply locally at each cross section. From Eq. (2.34), the variation of the tube radius R can be expressed as

$$\frac{dR}{dx} = k \frac{dp}{dx}. \quad (2.35)$$

Then, since $\alpha = -dp/dx$, Eq. (2.13) reduces to

$$Q = \frac{\pi R^4}{8\eta} \frac{-dR/dx}{k} = -\frac{\pi}{8\eta} \frac{dR^5/dx}{5k}, \quad (2.36)$$

where η is the viscosity of the Newtonian fluid. Since the flow rate Q is constant along the x -axis, R^5 is found to be a linear function of x . If the radii of the tube at the inlet and outlet are expressed as R_a and R_v , respectively, and the disturbances due to entry and exit are assumed to be negligible, then the radius of the tube, $R(x)$, can be expressed as

$$R^5 = R_a^5 - \frac{R_a^5 - R_v^5}{L}x, \quad (2.37)$$

where L is the length of the tube, and R_a and R_v are related to the pressures upstream and downstream, p_a and p_v , respectively, as

$$R_a = R_0 + kp_a, \quad R_v = R_0 + kp_v. \quad (2.38)$$

Then, from Eqs. (2.37) and (2.36) we have the tube radius and flow rate:

$$R = \left[R_a^5 - \frac{R_a^5 - R_v^5}{L}x \right]^{\frac{1}{5}}, \quad (2.39)$$

$$Q = Q_0 \left(1 - \left(\frac{R_v}{R_a} \right)^5 \right), \quad Q_0 = \frac{\pi R_a^5}{40\eta kL}. \quad (2.40)$$

Figure 2.10b shows Q/Q_0 versus R_v/R_a . It is seen that $Q/Q_0 \approx 1$ for a rather wide range of R_v/R_a from 0 to ~ 0.5 . Since Q_0 is independent of the downstream condition, this implies that the flow rate is mainly determined by the upstream condition,

unless $R_v/R_a \approx 1$. This feature exhibits a sharp contrast to the flow through a rigid tube, where the flow rate is proportional to the pressure difference, $\Delta p (= p_a - p_v)$.

The solutions (2.39) and (2.40) are obtained based on the linear relationship between tube radius and pressure difference (2.34). Instead of this assumption, we may adopt Hooke's law for the dilatation of the tube (Fung 1996).

Noting that the circumferential stress in the tube wall of thickness h is expressed as pR/h by Laplace's law, we have an expression for Hooke's law in terms of Young's modulus E :

$$\frac{pR}{h} = E \left(\frac{R}{R_0} - 1 \right). \quad (2.41)$$

Here, we assume E , h and R_0 are constant. Inserting this expression into Eq. (2.13) yields

$$-\frac{dp}{dx} \left(1 - \frac{R_0}{hE} p \right)^{-4} = \frac{8\eta}{\pi R_0^4} Q. \quad (2.42)$$

Since all quantities except $p(x)$ are constant, Eq. (2.42) can be integrated to obtain the solution in terms of tube radii at the inlet and outlet, R_a and R_v , respectively,

$$Q = Q_0 \left(1 - \left(\frac{R_v}{R_a} \right)^3 \right), \quad Q_0 = \frac{\pi h E R_a^3}{24 \eta L}. \quad (2.43)$$

This equation is similar to Eq. (2.40) and has a similar feature, i.e., the flow rate does not depend linearly on pressure difference, Δp , and instead depends mostly on the upstream condition.

2.2 Vascular Solid Mechanics

Mechanical stress is one of the factors that regulate the behavior of blood vessels (Hayashi et al. 2001; Humphrey 2002). It affects the physiological and pathological responses of the vascular wall. Macroscopically, mechanical stress can cause a vascular wall to rupture. Microscopically, it can trigger responses in the mechanoreceptors of vascular cells. This section focuses on the macroscopic effects of mechanical stress on the vascular wall.

2.2.1 Fundamentals of Solid Mechanics

There are two approaches to studying the mechanics of the vascular wall: one involves formulating an equation to balance force to obtain the stress, and the other formulates a stress-strain relationship for the vascular wall and solves a boundary-value problem for a large deformation of the blood vessel.

Considering the first approach, Laplace's law can be applied to a membrane, which has negligible resistance to deformation with bending (Fung 1993). Denoting the principal curvatures and tensions (force per unit length) as κ_i and T_i ($i = 1, 2$), respectively, and the pressures on the inner and outer wall as p_i and p_0 , Laplace's equation is expressed as

$$T_1\kappa_1 + T_2\kappa_2 = p_i - p_0 \quad (2.44)$$

where κ_i is related to the principal radius of curvature r_i as

$$r_1 = 1/\kappa_1, \quad r_2 = 1/\kappa_2. \quad (2.45)$$

For a thin cylindrical tube with inner diameter d_i and wall thickness t subjected to intraluminal pressure p ($p_0 = 0$), the relations

$$r_1 = d_i/2, \quad r_2 = \infty \quad (2.46)$$

hold. Therefore, Laplace's equation can be written as

$$2T_1/d_i = 2\sigma t/d_i = p \quad (2.47)$$

where σ is the average of the circumferential stress (hoop stress) distributed over the wall thickness.

The other approach to revealing the mechanics of the vascular wall involves formulating a stress-strain relationship for the vascular wall and solves a boundary-value problem for a large deformation of the blood vessel. To solve the problem, finite deformation theory is introduced from continuum mechanics (Holzapfel 2000).

Consider the Cartesian coordinate system $O-x_1x_2x_3$. A particle at an initial position \mathbf{X} in a body at time $t = 0$ moves to its current position \mathbf{x} at time $t = t$ with deformation of the body. Using basis vectors \mathbf{e}_i and components X_i and x_i ($i = 1, 2, 3$), the initial and current positions \mathbf{x} and \mathbf{X} are expressed as

$$\mathbf{X} = X_i\mathbf{e}_i = X_1\mathbf{e}_1 + X_2\mathbf{e}_2 + X_3\mathbf{e}_3, \quad \mathbf{x} = x_i\mathbf{e}_i = x_1\mathbf{e}_1 + x_2\mathbf{e}_2 + x_3\mathbf{e}_3 \quad (2.48)$$

where the repeat of the dummy index i obeys the summation convention.

We assume that the relations

$$\mathbf{x} = \mathbf{x}(\mathbf{X}, t), \quad \mathbf{X} = \mathbf{X}(\mathbf{x}, t) \quad (2.49)$$

hold. The deformation gradient \mathbf{F} , a two-point tensor, is defined as

$$\mathbf{F} = F_{ij}\mathbf{e}_i \otimes \mathbf{e}_j = \frac{\partial \mathbf{x}}{\partial \mathbf{X}} = \frac{\partial x_i}{\partial X_j}\mathbf{e}_i \otimes \mathbf{e}_j \quad (2.50)$$

where the symbol \otimes indicates a tensor product.

The inverse of \mathbf{F} is obtained as

$$\mathbf{F}^{-1} = \frac{1}{\det \mathbf{F}} \left(\frac{1}{2} e_{jkl} e_{imn} F_{km} F_{ln} \right) \mathbf{e}_i \otimes \mathbf{e}_j \quad (2.51)$$

where e_{ijk} is a permutation symbol defined as

$$e_{ijk} = \begin{cases} 1, & (i, j, k) = (1, 2, 3), (2, 3, 1), (3, 1, 2) \\ -1, & (i, j, k) = (3, 2, 1), (2, 1, 3), (1, 3, 2) \\ 0, & i = j \text{ or } j = k \text{ or } k = i \end{cases} \quad (2.52)$$

and the determinant of \mathbf{F} is calculated as

$$\det \mathbf{F} = e_{ijk} F_{1i} F_{2j} F_{3k}. \quad (2.53)$$

A transpose of \mathbf{F} is expressed as

$$\mathbf{F}^T = F_{ij}^T \mathbf{e}_i \otimes \mathbf{e}_j = F_{ij} \mathbf{e}_j \otimes \mathbf{e}_i = \frac{\partial x_i}{\partial X_j} \mathbf{e}_j \otimes \mathbf{e}_i = \frac{\partial x_j}{\partial X_i} \mathbf{e}_i \otimes \mathbf{e}_j. \quad (2.54)$$

The right Cauchy-Green deformation tensor \mathbf{C} and the left Cauchy-Green deformation tensor \mathbf{B} are defined as

$$\mathbf{C} = \mathbf{F}^T \mathbf{F}, \quad \mathbf{B} = \mathbf{F} \mathbf{F}^T \quad (2.55)$$

Therefore, the components of the above deformation tensors can be written as

$$\mathbf{C} = \left(\frac{\partial x_k}{\partial X_i} \frac{\partial x_k}{\partial X_j} \right) \mathbf{e}_i \otimes \mathbf{e}_j, \quad \mathbf{B} = \left(\frac{\partial x_i}{\partial X_k} \frac{\partial x_j}{\partial X_k} \right) \mathbf{e}_i \otimes \mathbf{e}_j. \quad (2.56)$$

Green's strain tensor \mathbf{E} is defined in the reference configuration as

$$\mathbf{E} = E_{ij} \mathbf{e}_i \otimes \mathbf{e}_j = \frac{1}{2} (\mathbf{C} - \mathbf{I}) = \frac{1}{2} (C_{ij} - \delta_{ij}) \mathbf{e}_i \otimes \mathbf{e}_j \quad (2.57)$$

where \mathbf{I} is a second-order unit tensor and δ_{ij} is Kronecker delta defined as

$$\mathbf{I} = \delta_{ij} \mathbf{e}_i \otimes \mathbf{e}_j \quad (\delta_{ij} = 1 \text{ if } i = j \text{ and } \delta_{ij} = 0 \text{ if } i \neq j). \quad (2.58)$$

The first, second, and third invariants of the right Cauchy-Green deformation tensor \mathbf{C} are defined as

$$I_1 = \text{tr} \mathbf{C} = C_{ii} \quad (2.59)$$

$$I_2 = \frac{1}{2} (\text{tr}^2 \mathbf{C} - \text{tr} \mathbf{C}^2) = \frac{1}{2} (C_{ii} C_{jj} - C_{ij} C_{ji}) \quad (2.60)$$

$$I_3 = \det \mathbf{C} \quad (2.61)$$

If \mathbf{v} is a velocity vector and v_i is its component, the material time derivative of variable \mathbf{A} is defined as

$$\dot{\mathbf{A}}(x, t) = \frac{\partial \mathbf{A}}{\partial t} + \frac{\partial \mathbf{A}}{\partial x_i} v_i. \quad (2.62)$$

The deformation rate tensor \mathbf{D} and spin tensor \mathbf{W} are defined as

$$\begin{aligned} \mathbf{D} &= \frac{1}{2} \left\{ \frac{\partial \mathbf{v}}{\partial \mathbf{x}} + \left(\frac{\partial \mathbf{v}}{\partial \mathbf{x}} \right)^T \right\} = \frac{1}{2} \{ \dot{\mathbf{F}} \mathbf{F}^{-1} + (\dot{\mathbf{F}} \mathbf{F}^{-1})^T \} \\ &= \frac{1}{2} \left(\frac{\partial v_i}{\partial x_j} + \frac{\partial v_j}{\partial x_i} \right) \mathbf{e}_i \otimes \mathbf{e}_j \end{aligned} \quad (2.63)$$

$$\begin{aligned} \mathbf{W} &= \frac{1}{2} \left\{ \frac{\partial \mathbf{v}}{\partial \mathbf{x}} - \left(\frac{\partial \mathbf{v}}{\partial \mathbf{x}} \right)^T \right\} = \frac{1}{2} \{ \dot{\mathbf{F}} \mathbf{F}^{-1} - (\dot{\mathbf{F}} \mathbf{F}^{-1})^T \} \\ &= \frac{1}{2} \left(\frac{\partial v_i}{\partial x_j} - \frac{\partial v_j}{\partial x_i} \right) \mathbf{e}_i \otimes \mathbf{e}_j. \end{aligned} \quad (2.64)$$

2.2.2 Structure and Components of Vascular Walls

In the order of the blood circulation, blood vessels are classified as the aorta (main artery), arteries, arterioles, capillaries, venules, veins, and the vena cava (Burton 1954; Rhodin 1979). Typical dimensions and intraluminal pressures for these vessels are listed in Table 2.1 (Mashima 1986; Berne and Levy 1993).

Blood vessels consist of fiber components; *i.e.*, elastic and collagen fibers, ground substances, and cellular components such as endothelial and smooth muscle cells (SMCs). The elastic and collagen fibers are load-bearing components. Elastic fibers are extensible, while collagen fibers are stiff. SMCs generate a contractile force to shrink muscular arteries.

The aorta, arteries, veins, and the vena cava have load-bearing structures. The vascular walls of these vessels consist of concentric layers called the intima, media, and adventitia. The intima is a thin layer, which comprises endothelial cells at the

Table 2.1 Typical dimensions and pressure of blood vessels (Burton 1954; Mashima 1986; Berne and Levy 1993)

Vessel	Diameter	Wall thickness	Pressure (mmHg)
Aorta	25 mm	2 mm	120–80
Artery	4 mm	1 mm	120–80
Arteriole	30 μm	6 μm ^(*)	60–40
Capillary	8 μm	0.5 μm ^(*)	30(–15)
Venule	20 μm	1 μm ^(*)	15(–10)
Vein	5 mm	0.5 mm	10(–5)
Vena cava	30 mm	1.5 mm	5–0

100 mmHg = 13.3 kPa. ^(*) The listed values (Berne and Levy 1993) differ from those in Burton (1954)

luminal surface and an internal elastic lamina at the boundary with the media. The media is the major region of the vascular wall. The media of the aorta and elastic arteries has a multilayer structure with an elastic lamina. Muscular arteries have a large number of smooth muscle cells, which generate force actively, mainly in the circumferential direction. The adventitia is the outermost layer of the vascular wall and connects the vascular wall to the surrounding tissues.

2.2.3 Mechanics of Normal Arterial Walls

We focus on the mechanics of the aorta and arteries. These vascular walls are subjected to blood pressure and longitudinal stretch. The luminal surface of the blood vessels are subjected to the blood pressures listed in Table 2.1 and the pressure of the blood column, for which the reference level is located at the height of the heart. Posture primarily affects the blood pressure in the lower limbs (Thubrikar 2007). If a blood vessel is located at heart level, the intraluminal pressure equals the value in Table 2.1.

2.2.3.1 Structure

Two types of multilayer wall model have been proposed (von Maltzahn et al. 1981; Yamada et al. 1999; Holzapfel et al. 2000; Matsumoto et al. 2004). One type of model includes the intima, media, and adventitia. The intima of the aorta/arteries is thickened physiologically in elderly people, while it is very thin in the young. The other type of model comprises alternate elastic and SMC layers in the media. A homogeneous single-layer wall model is the simplest and most commonly used model.

2.2.3.2 Geometry

The arterial tree includes straight, curved, and branched portions. The transverse cross-section of the vascular wall is almost circular and the wall thickness can vary along the circumference. Such variation occurs as a result of the remodeling of vascular tissues in a variety of environments.

The simplest geometrical model is a hollow cylinder. Realistic patient-specific models can also be built using image slices obtained with magnetic resonance imaging (MRI) or computed tomography (CT) (Tang et al. 2009). A model is subject-specific if the dimensions of a specimen are measured from an actual body using any technique.

2.2.3.3 Incompressibility

The vascular wall is nearly incompressible because of its high water content (Carew et al. 1968; Chuong and Fung 1984). The incompressibility condition is expressed as

$$I_3 = \det \mathbf{C} = 1 \quad \text{or} \quad J = \det \mathbf{F} = 1. \quad (2.65)$$

This incompressibility constraint is added to an equation for an incompressible strain energy density function as $H/2 \cdot (I_3 - 1)$, where H is a Lagrange multiplier or an indeterminate pressure, which is determined by the boundary conditions. An example showing how to calculate H is given in Sect. 2.2.3.5.

2.2.3.4 Passive and Active Mechanical Properties

The stress-strain relationship of the arteries depends on the direction of deformation. It tends to be isotropic in the portion near the heart and anisotropic (orthotropic or transversely isotropic) peripherally (Azuma and Hasegawa 1971).

Elastic and collagen fibers are passive components, while smooth muscle is an active component. In a passive state, the vascular wall behaves as a nonlinear viscoelastic material. In an active state, generation of a contractile force in the smooth muscle reduces the vascular diameter (Murphy 1980). The effect of smooth muscle contraction is strong for muscular arteries; *e.g.*, the renal and femoral arteries, and weak for elastic arteries; *e.g.*, the carotid artery (Cox 1978). The maximum contractile force depends on the length of the smooth muscle (Murphy 1976).

2.2.3.5 Constitutive Equations

Hyperelastic, viscoelastic, and poroelastic models have been proposed (Vito and Dixon 2003). Of these, incompressible hyperelastic models are used most frequently. One postulates a strain energy density function in a stress-free configuration. Unloaded and stress-free configurations should be distinguished because a vascular wall can change its geometry by releasing any residual stress (See Fig. 2.11) (Fung 1993).

An isotropic, transversely isotropic, or orthotropic incompressible strain energy function is introduced and applied to a hollow cylinder representing a blood vessel. Stresses are calculated under physiological loads; *i.e.*, a constant axial stretch, λ_z , and a uniform intraluminal pressure, p . The residual strain component in the

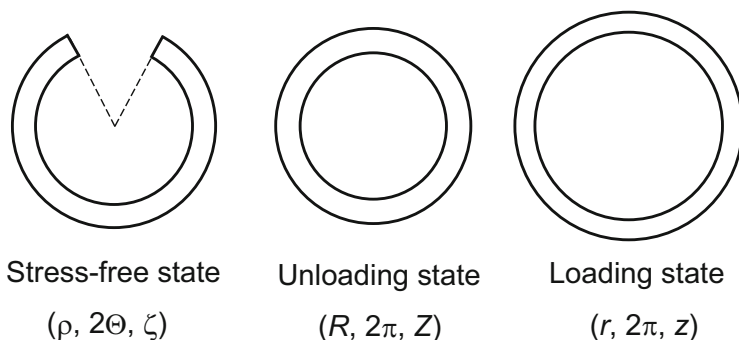


Fig. 2.11 Transverse cross-sections of a hollow cylindrical vessel in the stress-free, unloaded, and loaded states. The corresponding radius, central angle, and longitudinal-axis coordinates are shown in each state (Note that the stress-free geometry is an assumption)

circumferential direction is assumed as a function of the position along the wall thickness.

Under axisymmetric deformation of a hollow cylinder, the radial, circumferential, and longitudinal directions are the principal directions. Then, the principal stretches in these three directions are defined respectively as

$$\lambda_r = \frac{dR}{d\rho}, \quad \lambda_\theta = \frac{\pi R}{\Theta \rho}, \quad \lambda_z = \frac{Z}{\zeta} \quad (\text{unloaded state}) \quad (2.66)$$

$$\lambda_r = \frac{dr}{d\rho}, \quad \lambda_\theta = \frac{\pi r}{\Theta \rho}, \quad \lambda_z = \frac{z}{\zeta} \quad (\text{loaded state}). \quad (2.67)$$

If there is no residual stress, the relationships

$$\Theta = \pi, \quad \rho = R, \quad \zeta = Z \quad (2.68)$$

hold. Therefore, the stretches can be written as

$$\lambda_r = \frac{dr}{dR}, \quad \lambda_\theta = \frac{r}{R}, \quad \lambda_z = \frac{z}{Z} \quad (\text{loaded state, no residual stress}). \quad (2.69)$$

Based on a vascular wall with a constant volume, the radius in a loaded state is expressed as

$$r = \sqrt{r_i^2 + \frac{\Theta(\rho^2 - \rho_i^2)}{\pi\lambda_z}} \quad (\rho_i < \rho_0), \quad r = \sqrt{r_i^2 + \frac{\Theta(\rho_i^2 - \rho^2)}{\pi\lambda_z}} \quad (\rho_i > \rho_0). \quad (2.70)$$

where the subscripts i and o denotes the inner (radius of the inner surface of the intima) and outer (radius of the outer surface of the adventitia) radius, respectively (Yamada 2012).

Since the radial, circumferential, and longitudinal directions are the principal directions, the incompressibility condition (Eq. 2.65) is written as

$$\lambda_r \lambda_\theta \lambda_z = 1. \quad (2.71)$$

An equilibrium equation in the radial direction is expressed as

$$\frac{d\sigma_r}{dr} + \frac{\sigma_r - \sigma_\theta}{r} = 0 \quad (2.72)$$

where σ_r and σ_θ are the Cauchy stress in the radial and circumferential directions, respectively. The boundary conditions are written as

$$\sigma_r = \begin{cases} -p & (r = r_i) \\ 0 & (r = r_o) \end{cases} \quad (2.73)$$

Then, the radial component of the Cauchy stress is calculated using

$$\sigma_r(r) = \int_{r_i}^r \frac{\sigma_\theta - \sigma_r}{r} dr - p. \quad (2.74)$$

The first and second invariants of \mathbf{C} are written as

$$I_1 = \lambda_r^2 + \lambda_\theta^2 + \lambda_z^2, \quad I_2 = \lambda_r^2 \lambda_\theta^2 + \lambda_\theta^2 \lambda_z^2 + \lambda_z^2 \lambda_r^2. \quad (2.75)$$

For an incompressible isotropic hyperelastic model, a strain energy density function is a function of I_1 and I_2 and the Cauchy stress components are written as

$$\begin{aligned} \sigma_r &= 2\lambda_r^2 \{W_1 + (\lambda_\theta^2 + \lambda_z^2)W_2\} + H \\ \sigma_\theta &= 2\lambda_\theta^2 \{W_1 + (\lambda_z^2 + \lambda_r^2)W_2\} + H \\ \sigma_z &= 2\lambda_z^2 \{W_1 + (\lambda_r^2 + \lambda_\theta^2)W_2\} + H \end{aligned} \quad (2.76)$$

where W_1 and W_2 are defined as

$$W_1 = \frac{\partial W(I_1, I_2)}{\partial I_1}, \quad W_2 = \frac{\partial W(I_1, I_2)}{\partial I_2}. \quad (2.77)$$

Vito and Hickey (1980) postulated that

$$W = b_1(I_1 - 3) + b_2(I_1 - 3)^2 + b_3(I_1 - 3)^3 + b_4(I_1 - 3)^4 \quad (2.78)$$

and Yamada et al. (1999) postulated that

$$W = C_1(I_1 - 3) + C_2(I_2 - 3) + C_3(I_2 - 3)^2 + C_4(I_2 - 3)^3 \quad (2.79)$$

as polynomials of the first and second invariants of \mathbf{C} where b_i and C_i ($i = 1, 2, 3, 4$) are material constants.

Substituting Eq. (2.76) into Eq. (2.74), the radial component of the Cauchy stress is expressed as

$$\sigma_r(r) = - \int_r^{r_o} \frac{2(\lambda_\theta^2 - \lambda_r^2)(W_1 + \lambda_z^2 W_2)}{r} dr = -L(r). \quad (2.80)$$

To optimize the set of material constants in a strain energy density function, one minimizes the error between the experimental (data points) and estimated (calculated points) curves. For each given pressure p , a value of the outer radius (or inner radius using Eq. (2.70)) should be determined to satisfy the relation

$$L(r_i) = p. \quad (2.81)$$

If an outer (inner) radius is given, the pressure p is calculated using Eq. (2.80). The stress components are obtained by

$$\begin{aligned}\sigma_r &= -L(r) \\ \sigma_\theta &= 2(\lambda_\theta^2 - \lambda_r^2)(W_1 + \lambda_z^2 W_2) - L(r) \\ \sigma_z &= 2(\lambda_z^2 - \lambda_r^2)(W_1 + \lambda_\theta^2 W_2) - L(r)\end{aligned}\quad (2.82)$$

In the longitudinal direction, the equation for the balance of force

$$F_z + \pi r_i^2 p = 2\pi \int_{r_i}^{r_o} \sigma_z r dr \quad (2.83)$$

holds, where F_z is the force in the longitudinal direction. For an incompressible isotropic hyperelastic model, the longitudinal force can be calculated as

$$F_z = 2\pi \int_{r_i}^{r_o} \{2(\lambda_z^2 - \lambda_r^2)(W_1 + \lambda_\theta^2 W_2) - (\lambda_\theta^2 - \lambda_r^2)(W_1 + \lambda_z^2 W_2)\} r dr. \quad (2.84)$$

As an incompressible orthotropic hyperelastic model, Chuong and Fung (1983) formulated an exponential type of strain energy density function

$$\begin{aligned}W &= \frac{C}{2} \exp Q \\ Q &= b_1 E_\theta^2 + b_2 E_z^2 + b_3 E_r^2 + 2b_4 E_\theta E_z + 2b_5 E_z E_r + 2b_6 E_r E_\theta\end{aligned}\quad (2.85)$$

in terms of the components of Green's strain tensor, which are expressed by the principal stretches as

$$E_r = \frac{1}{2}(\lambda_r^2 - 1), \quad E_\theta = \frac{1}{2}(\lambda_\theta^2 - 1), \quad E_z = \frac{1}{2}(\lambda_z^2 - 1). \quad (2.86)$$

The stress components and longitudinal force are expressed as

$$\begin{aligned}\sigma_r &= -L(r) \\ \sigma_\theta &= Ce^Q [(1 + 2E_\theta)\{b_1 E_\theta + b_4(\lambda_z^2 - 1)/2 + b_6 E_r\} \\ &\quad - (1 + 2E_r)\{b_3 E_r + b_5(\lambda_z^2 - 1)/2 + b_6 E_\theta\}] - L(r) \\ \sigma_z &= Ce^Q [\lambda_z^2 \{b_2(\lambda_z^2 - 1)/2 + b_4 E_\theta + b_5 E_r\} \\ &\quad - (1 + 2E_r)\{b_3 E_r + b_5(\lambda_z^2 - 1)/2 + b_6 E_\theta\}] - L(r)\end{aligned}\quad (2.87)$$

$$L(r) = C \int_r^{r_o} [(1 + 2E_\theta) \{b_1 E_\theta + b_4 (\lambda_z^2 - 1)/2 + b_6 E_r\} - (1 + 2E_r) \{b_3 E_r + b_5 (\lambda_z^2 - 1)/2 + b_6 E_\theta\}] (e^Q/r) dr \quad (2.88)$$

$$F_z = 2\pi C \int_{r_i}^{r_o} r e^Q [\lambda_z^2 \{b_2 (\lambda_z^2 - 1)/2 + b_4 E_\theta + b_5 E_r\} - (1 + 2E_r) \{b_3 E_r + b_5 (\lambda_z^2 - 1)/2 + b_6 E_\theta\}/2 - (1 + 2E_\theta) \{b_1 E_\theta + b_4 (\lambda_z^2 - 1)/2 + b_6 E_r\}/2] dr \quad (2.89)$$

In a loaded state, the resultant force of the circumferential Cauchy stress is balanced by the resultant intraluminal pressure as

$$\int_{r_i}^{r_o} \sigma_\theta dr = pr_i. \quad (2.90)$$

A comparison of the above equation with Laplace's equation (Eq. 2.47) shows that the circumferential stress in Eq. (2.47) is equal to an average of the circumferential stress over the wall thickness for a deformed blood vessel as

$$\sigma = \int_{r_i}^{r_o} \sigma_\theta dr / t. \quad (2.91)$$

Yamada et al. (2007) demonstrated the effect of residual strain on the circumferential stress over the wall thickness. They used the following strain energy density function

$$W = C_1(I_1 - 3) + C_2(I_1 - 3)^2 + C_3(I_1 - 3)^3. \quad (2.92)$$

They determined the material constants C_1 , C_2 , and C_3 , and the inner or outer radius in the stress-free state to reproduce the same pressure-diameter relationship for various cases of residual strain.

In the model, the opening angle Ψ is defined as

Table 2.2 Dimensions of an opened hollow cylindrical wall in the stress-free state and the material constants used to reproduce the same pressure-diameter relationship under a constant longitudinal stretch of 1.3 and intraluminal pressure (Yamada et al. 2007)

Ψ (degree)	r_i (mm)	r_o (mm)	C_1 (kPa)	C_2 (kPa)	C_3 (kPa)
0	2.6	3.5	12.0	8.0	37.5
60	5.0	4.1	9.9	11.3	38.1
100	7.3	6.4	8.3	12.8	37.2

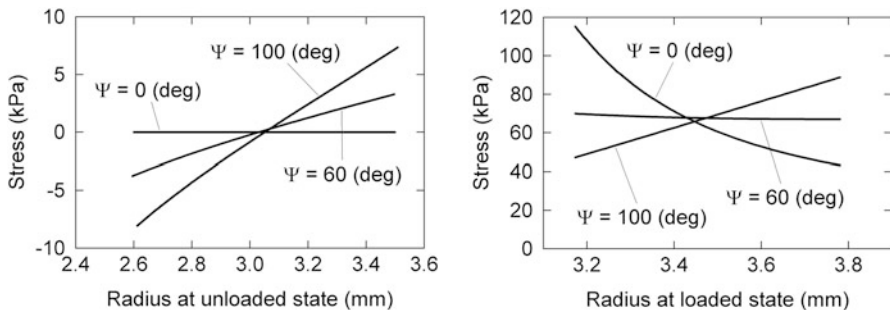


Fig. 2.12 Distributions of the circumferential stress in the unloaded stage (*left*) and loaded state under a longitudinal stretch of 1.3 and intraluminal pressure of 13 kPa (Modified from Yamada et al. 2007)

$$\Theta + \Psi = \pi. \quad (2.93)$$

The dimensions and material constants of the model were determined as shown in Table 2.2. Figure 2.12 shows the distributions of the circumferential component of the Cauchy stress in the unloaded and loaded states under the boundary conditions of a longitudinal stretch of 1.3 and an intraluminal pressure of 13 kPa (98 mmHg). The results indicate that an increase in the opening angle decreases the concentration of the circumferential stress at the intimal side of the wall, and a further increase causes a negative stress gradient across the wall thickness.

It is important to model the mechanical behavior of the active components; *i.e.*, the smooth muscles, to describe the mechanical behavior of blood vessels. The active force of skeletal muscles is modeled as a function of the length, velocity, and activation level. The following model of smooth muscles considers their length and activation (Yamada 1999).

The total Cauchy stress tensor of an active component is assumed to be the sum of the passive and active stresses or

$$\sigma_t = \sigma_p + \sigma_a. \quad (2.94)$$

The stress-strain relationship of the passive stress is formulated as

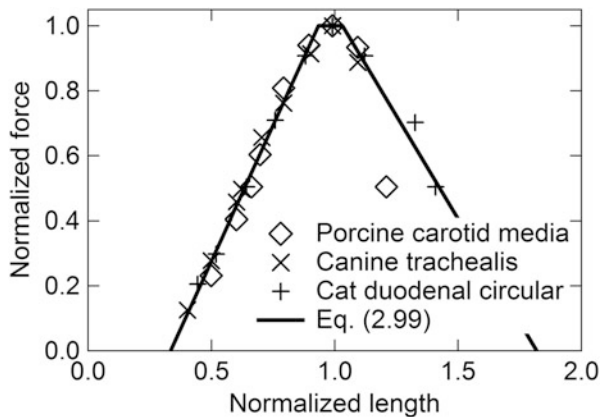
$$\hat{\sigma}_p = \kappa(\text{tr}\mathbf{D})\mathbf{I} + 2\mu\mathbf{D} \quad (2.95)$$

where κ and μ are Lamé constants. These constants are related to Young's modulus E and Poisson's ratio ν as

$$\kappa = \frac{E\nu}{(1+\nu)(1-2\nu)}, \quad \mu = \frac{E}{2(1+\nu)}. \quad (2.96)$$

The Jaumann time derivative of the passive stress is defined as

Fig. 2.13 Length dependence of the isometric maximum force of various smooth muscles (Murphy 1976) and a mathematical model (Eq. 2.99) formulated by Yamada (1999) (Modified from Yamada 1999)



$$\hat{\sigma}_p = \dot{\sigma}_p + \sigma_p W - W \sigma_p. \quad (2.97)$$

Active stress of smooth muscle that aligns in the direction of a unit vector \mathbf{m} and has a stretch of λ is formulated as a product of the activation level ξ and the length-dependent maximum stress τ_{\max} as

$$\sigma_a = \xi \tau_{\max}(\lambda) \mathbf{m} \otimes \mathbf{m} \quad (0 \leq \xi \leq 1) \quad (2.98)$$

where the first unit vector \mathbf{m} shows the direction of the stress component and the second \mathbf{m} shows the normal direction of the face on which the stress acts.

Based on Murphy's report (1976), Yamada (1999) determined the length-dependent maximum stress for smooth muscles as (Fig. 2.13)

$$\frac{\tau_{\max}(\lambda)}{\tau_{\max}(\lambda_{\max})} = \begin{cases} 1.67(\lambda/\lambda_{\max}) - 0.56, & 0.34 \leq \lambda/\lambda_{\max} \leq 0.93 \\ 1, & 0.93 < \lambda/\lambda_{\max} < 1.03 \\ -1.27(\lambda/\lambda_{\max}) + 2.31, & 1.03 \leq \lambda/\lambda_{\max} \leq 1.82 \\ 0, & \lambda/\lambda_{\max} < 0.34, \lambda/\lambda_{\max} > 1.82 \end{cases} \quad (2.99)$$

A finite element analysis was conducted using a model with nine concentric layers, including five passive and four active layers alternately, with the same thickness (Yamada et al. 1999). Figure 2.14 shows the stress distributions in the circumferential direction in the passive and active states and the change in the opening angle as an index of the residual strain with an increase in the activation level.

The simulation results indicate that activation decreases the circumferential stress of the passive components; *i.e.*, elastic and collagen fibers, and increases the stress of the active component; *i.e.*, smooth muscles. A comparison of Figs. 2.12 and 2.14 indicates that both the opening angle and contraction of smooth muscles change the gradient of circumferential stress of a homogeneous model in the

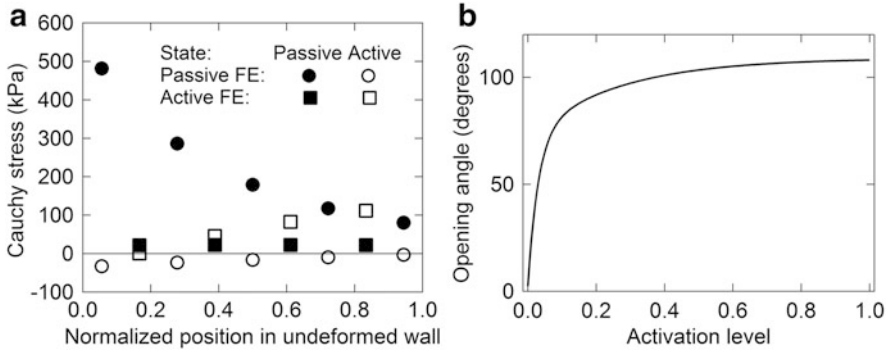


Fig. 2.14 (a) Distributions of the Cauchy stress in the circumferential direction in the passive and active states (activation level $\xi = 0$ and 1, respectively) for a nine-layer finite element model under a longitudinal stretch of 1.7 and an intraluminal pressure of 13 kPa. Residual stress is not considered. (b) Change in the opening angle, Ψ , which is defined at a stress-free vascular wall as an index of residual strain, with an increase in the activation level of ξ (Modified from Yamada et al. 1999)

negative direction. In other words, they cause the stress to decrease on the inner side and increase on the outer side.

2.2.4 Mechanics of Arterial Walls in Diseases

The structure, components, geometry, and accompanying mechanical properties of arterial walls change with age (Hayashi 1993; Nichols et al. 2011). Elderly people frequently develop arterial diseases such as atherosclerosis, aneurysms, and aortic dissection as a result of degeneration with aging.

2.2.4.1 Atherosclerosis

Atherosclerosis involves the accumulation of lipoproteins in a deep intimal layer and the development of a fibrous cap. The rupture of a plaque causes the formation of a thrombus, which can lead to ischemia or infarction. Many fluid and solid mechanics studies have examined atherosclerosis.

The earliest studies of atherosclerosis focused on the hemodynamic conditions that accelerate the invasion of low-density lipoproteins in the blood into the intima. In recent years, many researchers have investigated the stress state in plaque regions using the finite element method. They evaluated the possibility of plaque rupture or compared the stress between vulnerable and stable plaques or between ruptured and un-ruptured ones.

Yamada et al. (2010) conducted a finite element analysis of ring-like specimens of the common carotid artery with a plaque by releasing the stress by cutting the wall, as shown in Fig. 2.15. They demonstrated the deformation and stress distribution of the arterial wall under a cyclic intraluminal pressure of 0–13 kPa and a

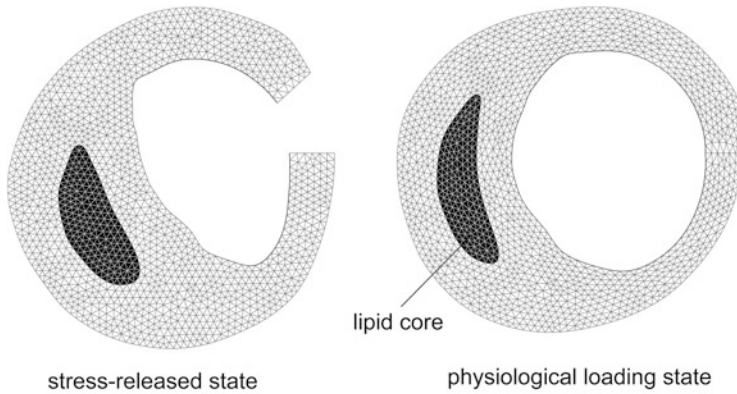


Fig. 2.15 Geometries of ring-like specimens of the common carotid artery in a stress-released state and under a physiological load with a longitudinal stretch of 1.07 and an intraluminal pressure of 13 kPa (Modified from Yamada and Sakata 2013)

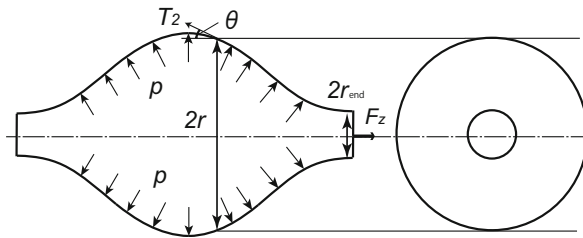


Fig. 2.16 The axisymmetric AAA model considered by Elger et al. (1996) (Modified from Yamada and Hasegawa 2007)

constant longitudinal stretch of 1.07. Yamada and Sakata (2013) observed a fluid-like lipid core. They modeled the lipid core using the bulk modulus of water and simulated a small change in pressure in the lipid core.

2.2.4.2 Aortic Aneurysms and Dissection

Abdominal aortic aneurysms (AAA) have frequently been investigated using solid mechanics. Two approaches can be used to estimate the stress in the aneurysm wall: one estimates the average stress based on the equilibrium of force, assuming a membrane-like aneurysm, and the other estimates the stress distribution using the equilibrium of stress and a constitutive equation, utilizing a finite element method.

Elger et al. (1996) assumed an axisymmetric spindle-like geometry for an AAA, as shown in Fig. 2.16, and formulated two equations for the equilibrium of force; *i. e.*, Laplace's Eq. (2.44), and, in the longitudinal direction,

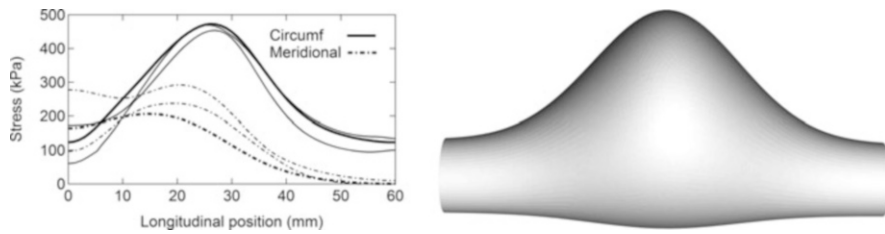


Fig. 2.17 Comparisons of the circumferential (*solid curve*) and meridional (*dot dashed curve*) components of the Cauchy stress using the results of equations for the force equilibrium (*thick lines*) and finite element analysis (*thin lines*: maximum and minimum values in the cross-sectional wall) along the median line on the side with the large bulge. The model has a maximum bulge with an inner diameter of 60 mm in the unloaded state at the origin (0 mm) of the longitudinal coordinate and ends at 60 mm (Modified from Yamada and Hasegawa 2007)

$$2\pi r T_2 \cos \theta = \pi(r^2 - r_{\text{end}}^2) p + F_z. \quad (2.100)$$

Yamada and Hasegawa (2007) extended this model to bilaterally symmetric AAA models to estimate the peak stress in the wall. They estimated the circumferential and meridional stresses along the anterior median line of the symmetric model using the two equations of force equilibrium and compared them with the results of a finite element analysis. This method provides a reasonable value and gives the location of the peak stress to evaluate the risk of wall rupture without utilizing the stress-free geometry and a constitutive equation (Fig. 2.17).

Aortic dissection follows an intimal tear and the penetration of blood into the delaminated space of the media in the longitudinal direction. An aortic dissection extends from the ascending to the descending thoracic aorta. This portion is subjected to pulsatile flow from the left ventricle. From the viewpoint of solid mechanics, the stress-strain relationship and mechanical strength have been investigated using the tensile loading and peeling tests (Okamoto et al. 2003; Holzapfel 2009; Pasta et al. 2012).

References

- Azuma T, Hasegawa M (1971) A rheological approach to the architecture of arterial walls. *Jpn J Physiol* 21(1):27–47
- Berne RM, Levy MN (1993) *Physiology*, 3rd edn. Mosby, St. Louis, p 362
- Burton AC (1954) Relation of structure to function of the tissues of the wall of blood vessels. *Physiol Rev* 34(4):619–642
- Carew TE, Vaishnav RN, Patel DJ (1968) Compressibility of the arterial wall. *Circ Res* 23(1):61–68
- Casson N (1959) A flow equation for pigment-oil suspensions of the printing ink type. In: Mill CC (ed) *Rheology of disperse systems*. Pergamon Press, Oxford, p 84
- Chien S (1970) Shear dependence of effective cell volume as a determinant of blood viscosity. *Science* 168:977–979

- Chuong CJ, Fung YC (1983) Three-dimensional stress distribution in arteries. *J Biomech Eng* 105 (3):268–274
- Chuong CJ, Fung YC (1984) Compressibility and constitutive equation of arterial wall in radial compression experiments. *J Biomech* 17(1):35–40. doi:[10.1016/0021-9290\(84\)90077-0](https://doi.org/10.1016/0021-9290(84)90077-0)
- Cokelet GR, Merrill EW, Gilliland ER, Shin H, Britten A, Wells RE Jr (1963) The rheology of human blood – measurement near and at zero shear rate. *Trans Soc Rheol* 7:303–317
- Cox RH (1978) Regional variation of series elasticity in canine arterial smooth muscles. *Am J Physiol* 234(5):H542–H551
- Elger DF, Blackketter DM, Budwig RS, Johansen KH (1996) The influence of shape on the stresses in model abdominal aortic aneurysms. *J Biomech Eng* 118(3):326–332. doi:[10.1115/1.2796014](https://doi.org/10.1115/1.2796014)
- Fahraeus R, Lindqvist T (1931) The viscosity of the blood in narrow capillary tubes. *Am J Physiol* 96:562–568
- Farber TE (1995) *Fluid dynamics for physicists*. Cambridge University Press, Cambridge
- Fung YC (1993) *Biomechanics: mechanical properties of living tissues*, 2nd edn. Springer, New York
- Fung YC (1996) *Biomechanics: circulation*, 2nd edn. Springer, New York
- Fung YC, Sobin SS (1972) Pulmonary alveolar blood flow. *Circ Res* 30:470–490
- Hayashi K (1993) Experimental approaches on measuring the mechanical properties and constitutive laws of arterial walls. *J Biomech Eng* 115(4):481–488. doi:[10.1115/1.2895528](https://doi.org/10.1115/1.2895528)
- Hayashi K, Stergiopoulos N, Meister J-J, Greenwald SE, Rachev A (2001) Techniques in the determination of the mechanical properties and constitutive laws of arterial walls. In: Leondes C (ed) *Biomechanical systems: techniques and applications*, vol. II, Cardiovascular techniques. CRC Press, Boca Raton
- Holzapfel GA (2000) *Nonlinear solid mechanics: a continuum approach for engineering*. Wiley, Chichester
- Holzapfel GA (2009) Arterial tissue in health and disease: experimental data, collagen-based modeling and simulation, including aortic dissection. In: Holzapfel G, Ogden R (eds) *Bio-mechanical modelling at the molecular, cellular and tissue levels*, vol 508. CISM International Centre for Mechanical Sciences. Springer, Vienna, pp 259–344. doi:[10.1007/978-3-211-95875-9_4](https://doi.org/10.1007/978-3-211-95875-9_4)
- Holzapfel GA, Gasser TC, Ogden RW (2000) A new constitutive framework for arterial wall mechanics and a comparative study of material models. *J Elast* 61(1–3):1–48. doi:[10.1023/A:1010835316564](https://doi.org/10.1023/A:1010835316564)
- Humphrey JD (2002) *Cardiovascular solid mechanics: cells, tissues, and organs*. Springer, New York
- Mashima H (1986) *Physiology*, 18th edn. Bunkodo, Tokyo, pp 396–397, in Jap
- Matsumoto T, Goto T, Sato M (2004) Microscopic residual stress caused by the mechanical heterogeneity in the lamellar unit of the porcine thoracic aortic wall. *JSME Int J, Ser A* 47 (3):341–348. doi:[10.1299/Jsmea.47.341](https://doi.org/10.1299/Jsmea.47.341)
- Merrill EW, Cokelet GC, Britten A, Wells RE Jr (1963) Non-Newtonian rheology of human blood –effect of fibrinogen deduced by “subtraction”. *Circ Res* 13:48–55
- Murphy RA (1976) Contractile system function in mammalian smooth muscle. *Blood Vessels* 13 (1–2):1–23
- Murphy RA (1980) Mechanics of vascular smooth muscle. In: *Handbook of physiology*. American Physiological Society, Bethesda, pp 325–351
- Nichols WW, O’Rourke MF, Vlachopoulos C (2011) *McDonald’s blood flow in arteries: theoretical, experimental and clinical principles*, 6th edn. Hodder Arnold, London, pp 411–446
- Oka S (1981) *Cardiovascular hemorheology*. Cambridge University Press, Cambridge
- Okamoto RJ, Xu HD, Kouchoukos NT, Moon MR, Sundt TM (2003) The influence of mechanical properties on wall stress and distensibility of the dilated ascending aorta. *J Thorac Cardiovasc Surg* 126(3):842–850. doi:[10.1016/S0022-5223\(03\)00728-1](https://doi.org/10.1016/S0022-5223(03)00728-1)

- Pasta S, Phillippi JA, Gleason TG, Vorp DA (2012) Effect of aneurysm on the mechanical dissection properties of the human ascending thoracic aorta. *J Thorac Cardiovasc Surg* 143 (2):460–467. doi:[10.1016/j.jtcvs.2011.07.058](https://doi.org/10.1016/j.jtcvs.2011.07.058)
- Pries AR, Secomb TW, Gaetgens P (2000) The endothelial surface layer. *Pflugers Arch - Eur J Physiol* 440:653–660
- Rhodin JAG (1979) Architecture of the vessel wall. In: Burne RM (ed) *Handbook of physiology*, sec 2, vol 2. American Physiological Society, Bethesda, pp 1–31
- Scott Blair GW (1959) An equation for the flow of blood, plasma and serum through glass capillaries. *Nature* 183:613–614
- Sugihara-Seki M (2006) Transport of spheres suspended in the fluid flowing between hexagonally arranged cylinders. *J Fluid Mech* 55:309–321
- Sugihara-Seki M, Fu BM (2005) Blood flow and permeability in microvessels. *Fluid Dyn Res* 37:82–132
- Tang DL, Teng ZZ, Canton G, Yang C, Ferguson M, Huang XY, Zheng J, Woodard PK, Yuan C (2009) Sites of rupture in human atherosclerotic carotid plaques are associated with high structural stresses – an in vivo MRI-based 3D fluid-structure interaction study. *Stroke* 40 (10):3258–3263. doi:[10.1161/Strokeaha.109.558676](https://doi.org/10.1161/Strokeaha.109.558676)
- Thubrikar MJ (2007) *Vascular mechanics and pathology*. Springer, New York
- Vito RP, Dixon SA (2003) Blood vessel constitutive models-1995-2002. *Annu Rev Biomed Eng* 5:413–439. doi:[10.1146/annurev.bioeng.5.011303.120719](https://doi.org/10.1146/annurev.bioeng.5.011303.120719)
- Vito RP, Hickey J (1980) The mechanical properties of soft tissues.2. The elastic response of arterial segments. *J Biomech* 13(11):951–957. doi:[10.1016/0021-9290\(80\)90166-9](https://doi.org/10.1016/0021-9290(80)90166-9)
- von Maltzahn WW, Besdo D, Wiemer W (1981) Elastic properties of arteries – a nonlinear two-layer cylindrical model. *J Biomech* 14(6):389–397. doi:[10.1016/0021-9290\(81\)90056-7](https://doi.org/10.1016/0021-9290(81)90056-7)
- Weinbaum S, Zhang X, Han Y, Vink H, Cowin SC (2003) Mechanotransduction and flow across the endothelial glycocalyx. *PNAS* 100:7988–7995
- Weinbaum S, Tarbell JM, Damiano ER (2007) The structure and function of the endothelial glycocalyx layer. *Annu Rev Biomed Eng* 9:121–167
- Whitmore RL (1968) *Rheology of the circulation*. Pergamon, Oxford
- Yamada H (1999) A mathematical model of arteries in the active state (Incorporation of active stress and activation parameter). *JSME Int J, Ser C* 42(3):545–551
- Yamada H (2012) *Fundamental mechanics and biomechanics*. Corona Publishing, Tokyo, in Jap
- Yamada H, Hasegawa Y (2007) A simple method of estimating the stress acting on a bilaterally symmetric abdominal aortic aneurysm. *Comput Methods Biomech Biomed Engin* 10 (1):53–61. doi:[10.1080/10255840601086531](https://doi.org/10.1080/10255840601086531)
- Yamada H, Sakata N (2013) Low pressure condition of a lipid core in an eccentrically developed carotid atheromatous plaque: a static finite element analysis. *J Biorheol* 27(1):9–17. doi:[10.1007/s12573-012-0051-x](https://doi.org/10.1007/s12573-012-0051-x)
- Yamada H, Shinoda T, Tanaka E, Yamamoto S (1999) Finite element modeling and numerical simulation of the artery in active state. *JSME Int J, Ser C* 42(3):501–507
- Yamada H, Yoshitake Y, Iwata N (2007) Comparisons of the finite element analysis solutions and the analytical ones for various opening-angled arterial walls. In: *Proc Mech Eng Congress*, 2007 Japan, No. 07–1, vol. 5, pp 163–164, in Jap
- Yamada H, Yuri K, Sakata N (2010) Correlation between stress/strain and the retention of lipoproteins and rupture in atheromatous plaque of the human carotid artery: a finite element study. *J Biomech Sci Eng* 5(4):291–302

Vascular Engineering

New Prospects of Vascular Medicine and Biology with a
Multidiscipline Approach

Tanishita, K.; Yamamoto, K. (Eds.)

2016, VI, 401 p. 184 illus., 103 illus. in color., Hardcover

ISBN: 978-4-431-54800-3